Article

Hippocampal astrocytes encode reward location

Adi Doron[1], Alon Rubin[2], Aviya Benmelech-Chovav[1], Netai Benaim[1], Tom Carmi[1], Ron Refaeli[1], Nechama Novick[1], Tirzah Kreisel[1], Yaniv Ziv[2] & Inbal Goshen[1✉]

Astrocytic calcium dynamics has been implicated in the encoding of sensory information[1–5], and modulation of calcium in astrocytes has been shown to affect behaviour[6–10]. However, longitudinal investigation of the real-time calcium activity of astrocytes in the hippocampus of awake mice is lacking. Here we used two-photon microscopy to chronically image CA1 astrocytes as mice ran in familiar or new virtual environments to obtain water rewards. We found that astrocytes exhibit persistent ramping activity towards the reward location in a familiar environment, but not in a new one. Shifting the reward location within a familiar environment also resulted in diminished ramping. After additional training, as the mice became familiar with the new context or new reward location, the ramping was re-established. Using linear decoders, we could predict the location of the mouse in a familiar environment from astrocyte activity alone. We could not do the same in a new environment, suggesting that the spatial modulation of astrocytic activity is experience dependent. Our results indicate that astrocytes can encode the expected reward location in spatial contexts, thereby extending their known computational abilities and their role in cognitive functions.

In recent years, research revealed many roles for astrocytes in modulating neuronal activity as well as behaviour[6]. Intracellular astrocytic calcium elevations—a prominent signal in these cells—were widely studied in vitro and recent studies have investigated them in vivo as well (reviewed in refs. [1,11]). Different studies have shown that cortical astrocytes respond to specific sensory stimuli with calcium transients (for example, visual cortex[2] and the somatosensory cortex[4,5]). Anaesthesia reduces calcium signalling in astrocytes[12], but only a minority of studies have investigated astrocyte activity in awake animals, and only one in the hippocampus[13]. Nevertheless, direct manipulation of astrocyte calcium signalling was shown to modulate behaviour, thereby extending their role beyond sensory processing[8–10,14]. Astrocytic calcium signals are also affected by the general state of the organism: they are elevated during arousal[3,15,16], reduced during natural sleep[17] and regulated by neuromodulators in vivo[3,18,19]. However, longitudinal investigation of the real-time calcium activity of astrocytes in the hippocampus of awake mice is lacking, let alone during performance of a multisensory cognitive task.

Place cells, a subset of pyramidal neurons in the hippocampal CA1 region, fire when the animal is in a specific location in space[20] and are considered to be the neuronal underpinning of spatial memory. The neuronal representation of a given environment entails goal-related information[21]: when an animal navigates in a familiar environment, place cells exhibit over-representation of rewarded locations[22–26] with narrower and more stable tuning curves than for other locations[27]. Furthermore, a subgroup of neurons was shown to represent the reward, independent of its location[28]. After exposure to a new environment, the activity of CA1 place cells reconfigures to form a new map that is unique to that environment[29–31], enabling neuronal discrimination between distinct contexts[32,33]. Recent studies have also shown that subpopulations of inhibitory cells exhibit spatially tuned activity and are modulated by rewards[34], but the role of astrocytes in this context is unclear.

Hippocampal astrocytes have an important role in memory processes, as shown by us and others[9,14,35]; we therefore hypothesized that their activity will also be modulated during the performance of a spatial cognitive task. To investigate the calcium activity of astrocytes in CA1 during a spatial paradigm, we used two-photon calcium imaging of a population of astrocytes in this region as mice ran on a linear treadmill and navigated in a multimodal circular virtual environment to obtain water rewards. We show that astrocytes gradually increase their calcium activity towards the previously learnt reward location when mice explore a familiar environment. Moreover, decoders using calcium dynamics in populations of astrocytes enabled us to decode the location of the mouse within the virtual environment. When the mice were introduced into a new virtual environment differing in visual and tactile cues, the astrocytic population was less modulated by reward location. Furthermore, when the reward location was shifted within the familiar environment, we did not observe significant ramping. After additional training in the new environment or in the familiar context with the new reward location, ramping was re-established, suggesting that the activity elevation towards a rewarding location requires familiarity. Our results shed light on the computational abilities of astrocytes, their role in contextual discrimination and their contribution to cognitive functions.

[1]Edmond and Lily Safra Center for Brain Sciences (ELSC), The Hebrew University of Jerusalem, Jerusalem, Israel. [2]Department of Neurobiology, Weizmann Institute of Science, Rehovot, Israel. ✉e-mail: inbal.goshen@elsc.huji.ac.il
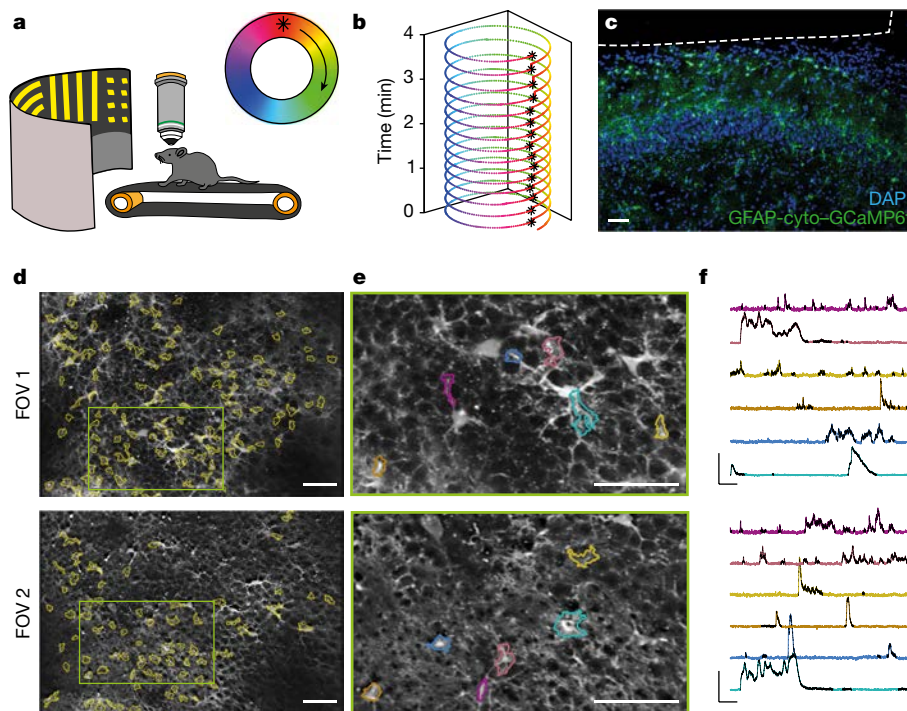
Fig. 1 | Ca²⁺ imaging of CA1 astrocytes in mice navigating a virtual reality. **a**, Experimental set-up. Head-fixed mice ran voluntarily on a linear treadmill to proceed in a circular virtual environment projected onto a round screen in front of them to obtain water rewards, constantly given at a specific location (asterisk). **b**, The trajectory of a well-trained mouse, completing 15 laps in 4 min. The mouse typically stops only after a reward is given. Asterisks denote reward delivery. **c**, Expression of GCaMP6f (green) in astrocytes in the CA1 after viral injection of AAV5-gfaABC1D-cyto-GCaMP6f. The imaging window was placed ~100 μm above the pyramidal cell layer, denoted by a white dashed line. **d**, Mean images of two FOVs acquired using a fast-z-tuneable lens, showing numerous segmented astrocytic ROIs. **e,f**, Magnified excerpts (**e**) from the fields shown in **d**, with example ROIs, and their corresponding activity traces (**f**). Detected events are shown in black. Scale bars, 50 μm (**c–e**), 30 s (**f**, horizontal) and 5 ΔF/F (**f**, vertical)).

Imaging CA1 astrocytes during navigation

To investigate the activity of a population of astrocytes while mice performed a spatial task, we combined two-photon calcium imaging with a custom-made circular virtual reality apparatus, and trained head-fixed mice to run on a linear treadmill belt (length, 170 cm) to obtain water rewards. A circular virtual environment with multiple distinct visual cues was projected onto a curved screen in front of them (Fig. 1a and Extended Data Fig. 1a). Mouse locomotion on the treadmill was recorded and translated into movement along the virtual track. A single water reward was given after completion of each 170 cm lap, matched with a specific location in the virtual environment (Fig. 1b).

We virally expressed cytosolic GCaMP6f in dorsal CA1 astrocytes, (Fig. 1c), enabling us to image calcium transients in astrocyte somata and main processes in a total of 11 mice. GCaMP was expressed in >92% (212 out of 230 cells from 3 mice) of CA1 astrocytes, with >94% specificity (212 out of 224 cells from 3 mice). Expression of GCaMP6f in somatostatin (SST)- or parvalbumin (PV)-positive cells or colocalization with the pan-neuronal marker NeuN was minimal (1.65% expression in neurons, 11 out of 668 cells from 3 mice) (Extended Data Fig. 1b). To increase the number of astrocytic regions of interest (ROIs) imaged in each session, we acquired separate time series from two fields of view (FOVs) using an electrical fast tuneable lens focusing on different tissue depths (Fig. 1d,e and Supplementary Video 1). The obtained time series were motion-corrected, and ROIs were semi-automatically segmented in each FOV separately. The signal from each ROI was extracted and the ΔF/F traces were calculated and used for binary event detection (Fig. 1f and Methods). Adjacent ROIs were more correlated than further ones on average (Extended Data Fig. 1c), and the size of the ROI was positively correlated with its event probability (Extended Data Fig. 1d).

Astrocytic activity ramps towards a reward

Reward locations are over-represented by place cells in familiar environments[23–27], and a subgroup of hippocampal neurons encodes rewards independent of their location[28]. However, it is unknown whether astrocytes exhibit location- and reward-specific responses. To examine this question, we first investigated the overall activity of the astrocytic population as mice traversed a familiar environment, and found that it was characterized by synchronous activity epochs across many of the ROIs (Fig. 2a and Supplementary Video 2). We calculated the number of concurrent events as a function of the mouse location, and observed that it increased towards the known reward location (Fig. 2b). The number of concurrent events decreased during the stationary epochs that often occurred during reward consumption (Pearson's $r = -0.4 \pm 0.04$, permutation test, $P \le 0.006$, $n = 9$ mice) (Extended Data Fig. 2a,b). The modulation of the astrocytic population activity by location was apparent across laps and significantly different from shuffled data, both when testing the number of concurrent events as a function of location (Pearson's $r = 0.4 \pm 0.03$, permutation test, $P \le 0.024$, $n = 9$ mice; Supplementary Information) (Fig. 2c,d and Methods) and the mean ΔF/F as a function of location (Pearson's $r = 0.25 \pm 0.03$, permutation test, $P \le 0.018$, $n = 9$ mice) (Extended Data Fig. 2c). Furthermore, when we analysed the somata and the processes separately, we obtained similar results, indicating that the ramping activity is not limited to specific subcompartments of the astrocytes (Pearson's $r = 0.36 \pm 0.03$ and $r = 0.38 \pm 0.03$, permutation tests, $P < 0.001$ and $P < 0.05$ for all 8 mice, in the somata and processes, respectively; two-sided paired t-test, $t_7 = 0.92$, $P = 0.39$) (Extended Data Fig. 2d,e and Methods).

When the reward was given at random locations along the track, we did not observe ramping (Pearson's $r = 0.02 \pm 0.02$, permutation test, $P \ge 0.084$, $n = 3$ mice) (Extended Data Fig. 2f), indicating that
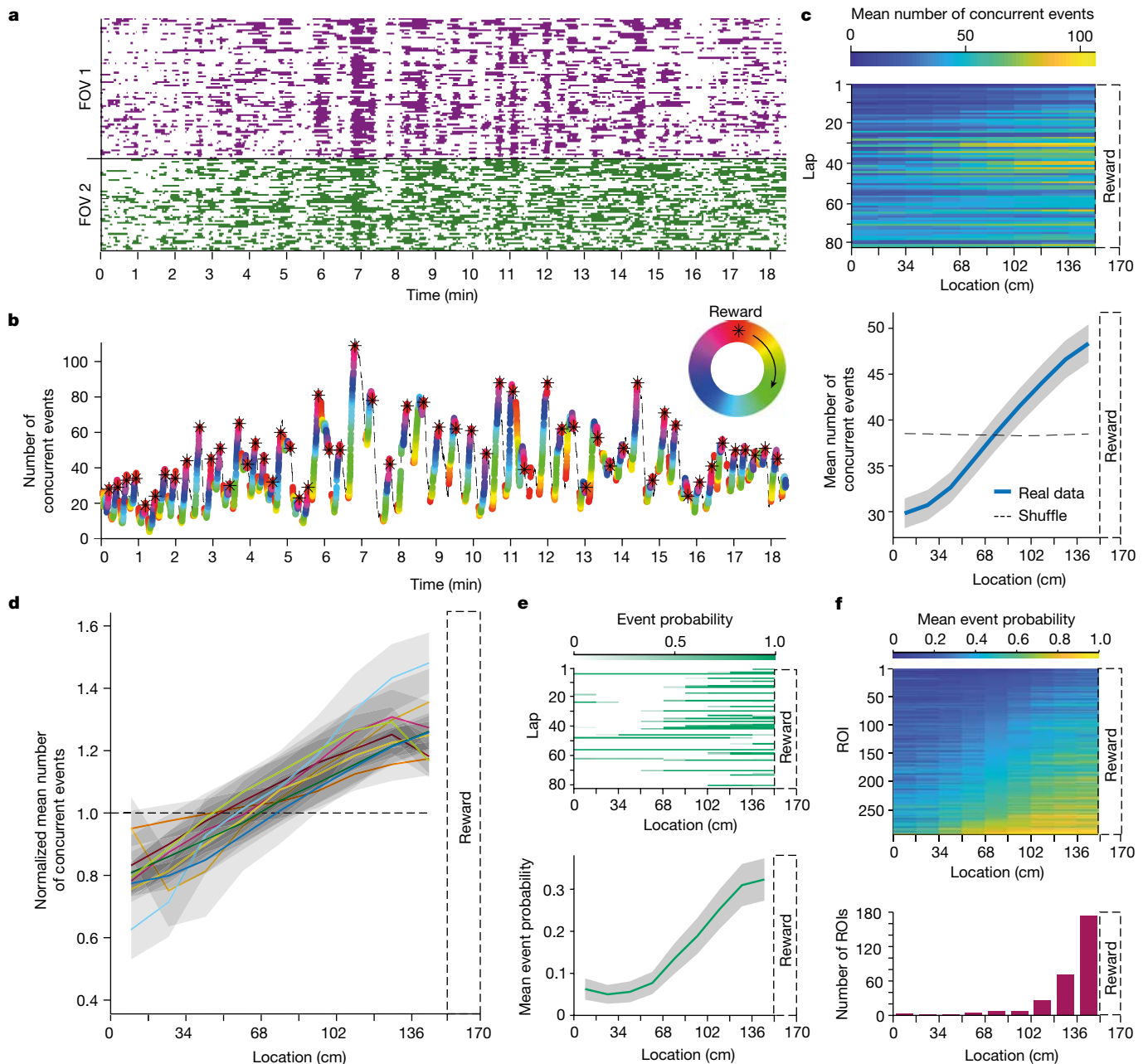
Fig. 2 | Astrocytic activity increases as mice move towards the reward location. a, Binary astrocytic Ca²⁺ traces acquired from ROIs in two FOVs when the mouse ran on the treadmill and advanced through the virtual reality. **b**, The sum of the binary traces (that is, the number of events per sampling point) shown in **a**. The height is the number of concurrent events, and the colours denote the mouse location along the track (the maze is shown in the top right). The astrocytic activity ramps as the mouse moves towards the known reward location, and decreases when the mouse is stationary. Asterisks denote reward delivery. The dashed line denotes stationary epochs. **c**, The mean number of concurrent events of the mouse in **a** and **b** as a function of binned locations in all laps (top), and averaged across laps (bottom), is significantly different from the shuffled data (Pearson's $r = 0.36$, one-sided permutation test, $P < 0.001$). **d**, The mean number of concurrent events as a function of location normalized by shuffled data in nine mice (the blue line represents the mouse shown in **c**), obtained from 972 ROIs, with 126, 86, 107, 107, 107, 114, 160, 72 and 93 ROIs from the individual mice. The observed ramping was significantly different from the shuffled data (one-sided permutation test, $P \leq 0.024$ in all 9 mice). **e**, Example of a ramping ROI, showing its event probability as a function of location and laps (top) and its mean event probability across laps (bottom). **f**, Mean event probability as a function of the location of ROIs with significant spatial information obtained from nine mice, sorted by the mean event probability in the central location bin (top). Most of these ROIs showed ramping, a gradual increase in mean activity probability apparent across laps, that peaked near the known reward location (bottom). For **c**–**e**, data are mean ± s.e.m. (shaded area).

the astrocytes do not encode the mouse position, but rather its location relative to the expected reward. When the virtual reality visual display was turned off, we still observed significant ramping in most mice (Pearson's $r = 0.2 \pm 0.04$, permutation test, $P \leq 0.009$ for $n = 3$ mice; Pearson's $r = 0.11$, permutation test, $P = 0.075$ for $n = 1$ mouse) (Extended Data Fig. 2g), suggesting that the tactile information is usually sufficient to induce astrocytic ramping in a familiar environment.

We next investigated whether, like place neurons, single astrocytic ROIs have activation peaks covering the entire environment with over-representation of the reward location. We found that about 30% (293 out of 972, from $n = 9$ mice) of the astrocytic ROIs had significant

Article

spatial information. However, their activation peaks did not tile the entire track; the maximal event probability of most of these ROIs was near the reward location, towards which they showed gradual ramping (Fig. 2e,f) indicating that astrocytes might represent the environment differently compared with neurons. This was also the case when we analysed the $\Delta F/F$ traces (23%; 225 out of 972 ROIs with significant spatial information from $n = 9$ mice) (Extended Data Fig. 2h).

The increase in astrocytic Ca^{2+} events towards the expected reward location may be the result of the mouse changing its velocity as it proceeds in the environment, as previous research has shown that astrocytes respond to locomotion in the cortex[16,17,36,37]. To test this, we first looked at the number of concurrent events in the astrocytic ROI population as a function of velocity. The correlation between astrocytic activity and velocity was weaker than between location and astrocytic activity across laps (Pearson's $r = 0.17 \pm 0.04$, permutation test, $P \geq 0.084$ in $n = 4$ mice, $P \leq 0.025$ in $n = 5$ mice) (Extended Data Fig. 2i,j). Moreover, when we investigated the interaction between location and velocity, we saw that the overall astrocytic activity varies more as a function of location in comparison to velocity (7.37 ± 0.74 and 3.62 ± 0.44 (mean $\pm$ weighted s.d.) for locations at a given velocity and velocities at a given location, respectively, paired t-test, $t_8 = 6.56$, $P = 0.0002$) (Extended Data Fig. 2k,l). Single astrocytic ROIs also exhibited higher variability across locations than across velocities (Extended Data Fig. 2m). Taken together, these findings suggest that the astrocytic signal is modulated by the reward location more than by the velocity of the mouse.

To further evaluate the unique contribution of location beyond other potential behavioural variables to the astrocytic activity, we used general linear models (Methods). Specifically, we fitted a linear model with five behavioural variables as inputs—normalized location, time since reward, velocity, recent distance run and licking—to predict the number of concurrent astrocytic events. The model performance was significantly better than that of a reduced model, which did not include the location as its input (log-likelihood ratio: 591.95 ± 188.33, likelihood ratio test, $P \leq 8.82 \times 10^{-14}$ in all $n = 9$ mice), as well as of models based on shuffled location data (coefficient of determination (r^2) between model prediction and the actual number of concurrent events: 0.25 ± 0.04 and 0.18 ± 0.03 for real and shuffled location inputs, respectively; permutation test, $P \leq 0.027$ in $n = 8$ mice, $P = 0.35$ in $n = 1$ mouse; paired t-test, $t_8 = 3.39$, $P = 0.0095$) (Extended Data Fig. 2n). Consistently, cross-validated models that included location as their input performed significantly better than reduced models (mean $r^2 = 0.21 \pm 0.04$ and 0.15 ± 0.03 in the full and reduced models, respectively; paired t-test, $t_8 = 3.5$, $P = 0.0081$; permutation test, $P < 0.004$ in $n = 8$ mice, $P = 0.065$ in $n = 1$ mouse) (Extended Data Fig. 2o).

We show here that astrocytic activity in the CA1 is modulated by reward location both when looking at single ROIs and at the entire imaged population. In contrast to place neurons, which fire selectively at specific locations throughout the entire space, the astrocytic activity gradually increases towards a single expected reward location.

Ramping requires previous experience

Previous studies have shown that CA1 place cells undergo global remapping after exposure to a new environment, and can discriminate between it and a familiar context[32,33]. Chronic imaging data of hippocampal astrocytes in awake behaving mice are lacking and, therefore, no such phenomenon is known in this population of cells. Hence, we examined whether ramping of astrocytic activity towards a rewarding location requires familiarity with the environment. To this end, we conducted chronic imaging of astrocytes both when mice navigated in a familiar environment, and when they were introduced into a new one, differing in tactile and visual cues (Extended Data Fig. 1a and Methods). We used fluorescence expression in sparse inhibitory neurons, enabling us to return to the same FOVs on subsequent days (Fig. 3a). First, only ROIs that were repeatedly active during both sessions were included in the

analysis (Fig. 3b). As expected, the subpopulation of repeatedly active astrocytic ROIs was significantly modulated by the location in the familiar environment, gradually increasing its overall activity towards the reward location (Fig. 3c). However, in the new environment, this ramping was less apparent (Pearson's $r = 0.41 \pm 0.03$ and $r = 0.2 \pm 0.05$ in the familiar and new environment, respectively, paired t-test, $t_6 = 8.04$, $P = 0.0002$) (Fig. 3d and Extended Data Fig. 3a). We also found significantly more ROI pairs with significant mutual information between their activity in the familiar environment compared with the new environment (proportion of significant mutual information ROI pairs: 0.39 ± 0.08 and 0.16 ± 0.04 in the familiar and new environment, respectively, paired t-test, $t_6 = 2.45$, $P = 0.049$) (Extended Data Fig. 3b,c). Second, we analysed all of the imaged ROIs (not just the repeated ones), and replicated the same results: reduced ramping in the new environment (Pearson's $r = 0.44 \pm 0.03$ and $r = 0.16 \pm 0.03$ in the familiar and new environment, respectively, paired t-test, $t_6 = 10.43$, $P = 0.00005$) (Extended Data Fig. 3d–f).

Next, we trained two mice in the new environment for an additional session, after which we found that ramping was re-established in the subpopulation of active and repeated ROIs (Pearson's $r = 0.44 \pm 0.07$, permutation test, $P \leq 0.031$, $n = 2$ mice) (Fig. 3e). We also tested the astrocytic activity when a different set of mice was re-exposed to the familiar context after the new one, and observed that the ramping was immediately apparent without additional training in the repeated and active ROIs (Pearson's $r = 0.31 \pm 0.11$, permutation test, $P \leq 0.004$, $n = 2$ mice) (Extended Data Fig. 3g), indicating that the exposure to the new context does not interfere with the familiar context representation.

Finally, we examined the astrocytic activity when the reward was shifted from its previously learnt location to a new one in a familiar environment. As expected, ramping was apparent when the reward was given in its original location (Pearson's $r = 0.54 \pm 0.11$, permutation test, $P \leq 0.002$, $n = 2$ mice) (Fig. 3f); however, it was not evident after the reward shift (Pearson's $r = 0.03 \pm 0.01$, permutation test, $P \geq 0.397$, $n = 2$ mice) (Fig. 3g). After training with the new reward location, significant ramping re-emerged in the repeatedly active ROIs (Fig. 3h) (Pearson's $r = 0.41 \pm 0.13$, permutation test, $P \leq 0.037$, $n = 2$ mice).

Taken together, our results indicate that the astrocyte population discriminates between contexts, showing ramping towards the expected reward in familiar, but not in new, environments. After learning of either a new environment or new reward location within a given context, ramping of astrocytic calcium activity emerges.

Decoding location from astrocytic activity

We next examined whether the activity of the astrocytic population would suffice to determine the location of the mouse along the track. To this end, we constructed a linear-regression decoder for each mouse that predicted its location on the basis of the binary calcium activity traces, or on shuffled traces as control (Fig. 4a–d and Extended Data Fig. 4). The decoders estimated the mice trajectories significantly better than when tested on shuffled data (mean error size: 44.4 ± 1.9 cm for real data, 59.5 ± 1.4 cm for shuffled data, $n = 6$ mice, paired t-test, $t_5 = 8.33$, $P = 0.0004$; Supplementary Information) (Fig. 4d and Methods).

Next, we examined whether similar linear decoders could infer the mouse location in the new environment (Fig. 4e–h). The performance of the decoders was not significantly different compared to when trained on shuffled data (mean error size: 52.3 ± 2.2 cm for real data, 55.9 ± 1.2 cm for shuffled data; paired t-test, $t_6 = 2.12$, $P = 0.079$; permutation test for individual decoder performance, $P \geq 0.066$ in $n = 7$ mice) (Fig. 4h). Their mean performance was significantly worse than the mean performance of the decoders trained and tested on the familiar environment (independent samples t-test, $t_{11} = 2.65$, $P = 0.023$). Finally, we trained separate linear decoders to predict the normalized velocity of the mice in the familiar environment on the basis of the binary Ca^{2+} activity traces, and found that their performance was not significantly different from decoders trained on shuffled data
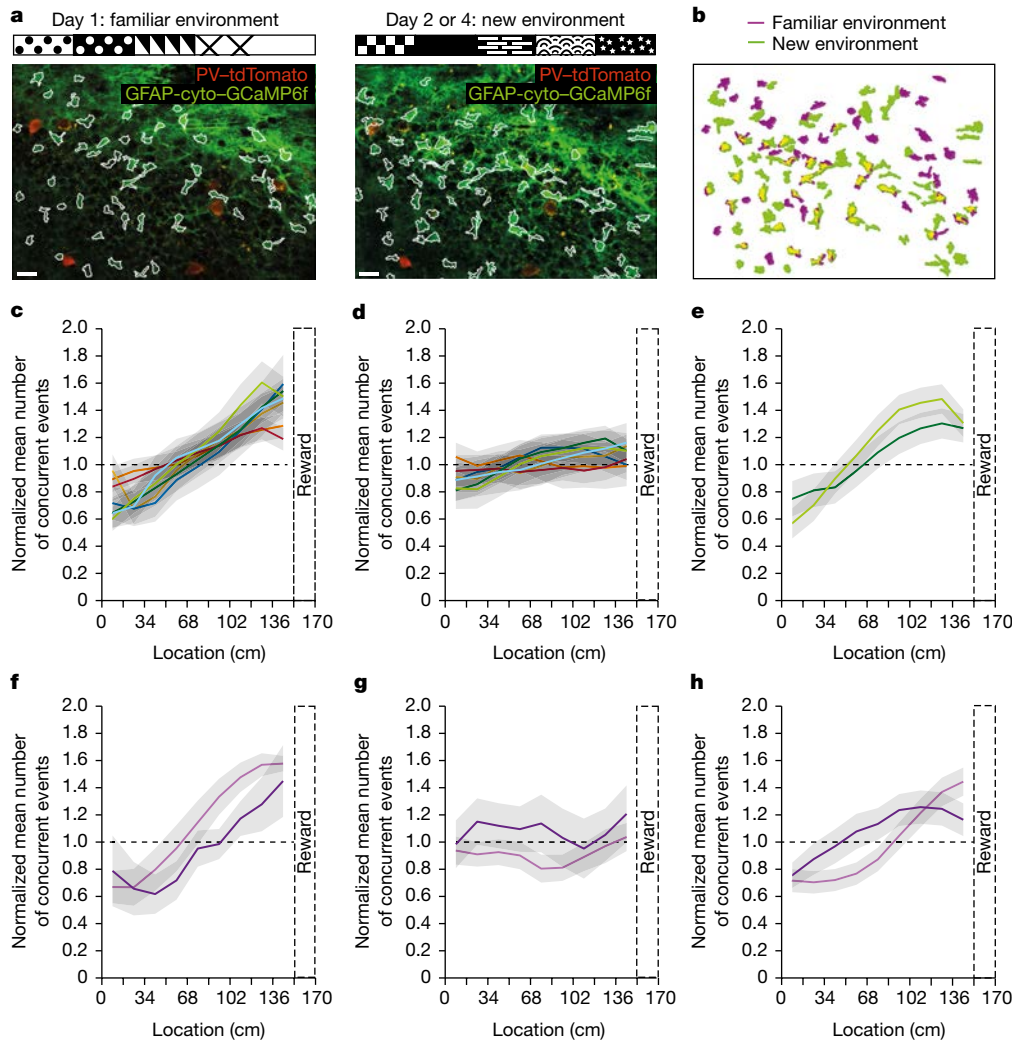
Fig. 3 | Astrocytic activity ramps as mice move towards the reward location in familiar environments, but not in new environments. a, Chronic imaging when mice navigated in familiar (left) and new (right) environments. Scale bars, 25 μm. The virtual environment walls are drawn at the top. The inhibitory neuronal tdTomato expression (here, PV neurons) was used to return to the same FOV on consecutive days. **b**, ROIs were segmented independently on each session, and their masks were registered. Only ROIs that were active during both sessions (shown in yellow) were included in the analysis. **c,d**, The normalized mean number of concurrent events as a function of location in the familiar environment (**c**) and in the new environment (**d**) for repeated active ROIs in seven mice. The correlation between location and astrocytic activity was significantly higher in the familiar environment compared with the new one (Pearson's $r = 0.41 \pm 0.03$ and $r = 0.2 \pm 0.05$ in the familiar and new environment, respectively; two-sided paired t-test, $t_6 = 8.04$, $P = 0.0002$).

e, Two mice were imaged for the third time in the new environment after an additional training day. The normalized mean number of concurrent events as a function of location shows that ramping was re-established after learning the new environment (Pearson's $r = 0.44 \pm 0.07$, one-sided permutation test, $P < 0.05$). **f,g**, The normalized mean number of concurrent events as a function of location shows ramping towards a known reward location in a familiar environment (Pearson's $r = 0.54 \pm 0.11$, one-sided permutation test, $P \le 0.01$) (**f**), which is eliminated once the reward is shifted to a new location in the same environment (Pearson's $r = 0.03 \pm 0.01$, one-sided permutation test, $P \ge 0.05$) (**g**). **h**, After additional training with the new reward location, the ramping is re-established (Pearson's $r = 0.41 \pm 0.13$, one-sided permutation test, $P < 0.05$). For **c**–**h**, data are mean ± s.e.m. (shaded area). Different mice are colour coded as in Fig. 2d.

(mean error size: 0.23 ± 0.02 for real traces, 0.23 ± 0.02 for shuffled data; paired t-test, $t_6 = 0.78$, $P = 0.472$; permutation test for individual decoder performance, $P \ge 0.138$ in $n = 6$ mice) (Fig. 4i–l), indicating that running velocity cannot be inferred from the astrocytic activity. Taken together, our findings demonstrate that reconstruction of mouse location trajectories from astrocytic activity using linear decoders requires familiarization with the environment and, as opposed to neurons[30], cannot be done in a new environment.

Discussion

Here we report longitudinal astrocytic activity in the hippocampus of awake behaving mice. We chronically imaged CA1 astrocytes while mice ran in familiar and new virtual environments. Although we noticed no 'place astrocytes' that tile the whole environment, we found that astrocytic activity shows persistent ramping towards the reward location, but only when both the spatial context and reward location within it were previously learnt. Furthermore, we demonstrate that astrocytic population activity alone can be used to reconstruct mouse trajectories in familiar environments. This is one of the first indications that astrocytes are involved in spatial tasks and can encode position-related information in familiar contexts, thereby extending their known roles in cognitive functions.

Our data indicate that astrocytes encode position-related information through gradual ramping towards the previously learnt reward location, both when examining the overall population and single ROI
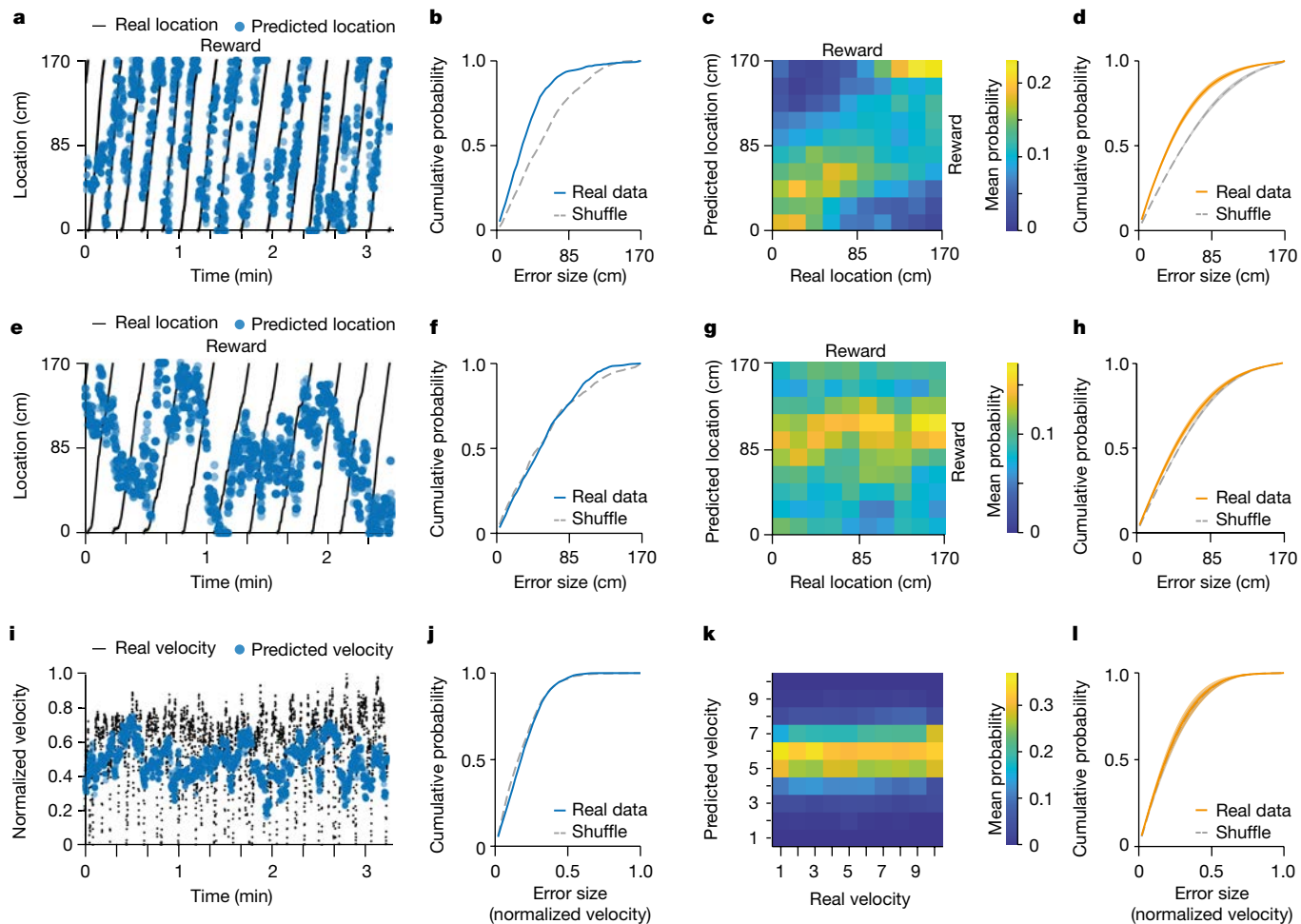
Fig. 4 | Decoding of mouse trajectory from astrocytic activity in the familiar environment. a–d, A linear regression decoder was trained to predict the location of mice in a familiar environment from binary astrocytic activity traces. **a,b,** An example mouse trajectory (black) overlaid with the predicted location (blue) (**a**), and its error cumulative probability plot (**b**). The decoder trained on real data outperformed the decoder trained on shuffled data. **c,** Mean confusion matrix of the mouse shown in **a** and **b**. The diagonally concentrated errors indicate that the predicted location is near the real location on average. **d,** Decoder mean error cumulative probability ($n = 6$ mice), showing that the location decoders performed significantly better when trained on real compared with shuffled data on average (two-sided paired t-test, $t_5 = 8.33$, $P = 0.0004$). **e–h,** Another decoder was trained to predict the location of mice in a new environment. **e,f,** An example trajectory of a mouse (black) overlaid with its inaccurately predicted location (blue) (**e**) and its error cumulative probability plot (**f**). The decoder trained on the real data performed similarly to the one trained on shuffled data. **g,** Mean confusion matrix of the

mouse shown in **i** and **j**. The horizontally concentrated errors indicate that the predicted location is independent of the real location on average. **h,** Decoder mean error cumulative probability ($n = 7$ mice), showing that the new location decoders were not significantly better when trained on real compared with shuffled data on average (two-sided paired t-test, $t_6 = 2.12$, $P = 0.079$). **i–l,** Another decoder was trained to predict mouse-normalized velocity. **i,j,** Example mouse velocity trace (black) overlaid with its inaccurately predicted velocity (blue) (**i**) and its error cumulative probability plot (**j**). The decoder trained on the real data performed similarly to the one trained on shuffled data. **k,** Mean confusion matrix of the mouse shown in **e** and **f**. The horizontally concentrated errors indicate that the predicted normalized velocity is independent of the real normalized velocity on average. **l,** Decoder mean error cumulative probability ($n = 6$ mice), showing the mean performance of the velocity decoders was not significantly better when trained on real compared with shuffled data on average (two-sided paired t-test, $t_6 = 0.78$, $P = 0.472$). For **d, h, l,** data are mean ± s.e.m. (shaded area).

activity. Such slow dynamics have been previously reported in neurons found in various brain regions[38–42] that are involved in motor planning, working memory and decision-making. Furthermore, prolonged dopamine signals showing persistent ramping towards a distant reward were found in the striatum[43,44]. Recently, a study has also shown that radial astrocytes of zebrafish gradually increase their calcium activity as the animals learn the ineffectiveness of their actions, triggering a behavioural shift to passivity[45]. Our results show that calcium activity in CA1 astrocytes is elevated towards the known reward location, consistent with a model in which astrocytic activity increases as evidence accumulates.

Our findings raise the question of what exactly the astrocytic ramping encodes. We show that, when the environment remains constant but the reward is shifted to a new location, ramping is eliminated, suggesting

that astrocytes encode the reward location, and not location per se. It is conceivable that the astrocytes encode various attributes of the reward, such as expectation, and the external environment serves only as cues leading towards it. It is therefore possible that, like certain neurons found in the hippocampus, astrocytes in this region may encode the progressions of sensory stimuli[46–48] or internal states (for example, motivation, expectation) that change with proximity to a goal. Although we studied the ramping of astrocytic activity towards a reward in a spatial context, future experiments can test whether this phenomenon also appears in non-spatial tasks. For example, when the reward appears after a learnt auditory sequence, such as tones in rising pitch, and is dissociated from a specific location in space.

By chronically imaging astrocytes, we were able to compare their activity when mice navigated a familiar environment and when they

were introduced into a new one, differing in visual and tactile cues. Notably, in the new environment, the astrocytic activity was no longer modulated by location, and it did not suffice to accurately decode the mouse trajectory. Place cells rapidly emerge in the CA1 after exposure to a new environment[49], and can be used to accurately decode the mouse location as early as on the first lap[30]. Our results suggest that the astrocytic representation of an environment develops more slowly than the neuronal one. Importantly, astrocytic activity is significantly different between familiar and new environments, which may indicate that astrocytes are involved in contextual discrimination, in conjunction with the neuronal representations[32,33]. Astrocytes are known to have slow temporal dynamics (although see ref. [5]), which may enable them to take part in computations that occur across long, behaviourally relevant time scales. Moreover, the fact that they receive inputs from multiple neurons may potentially enable them to serve as spatiotemporal integrators, as has been demonstrated in vitro[50] and in vivo[45]. Astrocytes were previously shown to encode sensory stimuli with calcium transients in the cortex and investigating the real-time involvement of hippocampal astrocytes in various behaviours will deepen our understanding of cognitive functions and their underlying computations.

Online content

Any methods, additional references, Nature Research reporting summaries, source data, extended data, supplementary information, acknowledgements, peer review information; details of author contributions and competing interests; and statements of data and code availability are available at https://doi.org/10.1038/s41586-022-05146-6.

1. Bazargani, N. & Attwell, D. Astrocyte calcium signaling: the third wave. *Nat. Neurosci.* **19**, 182–189 (2016).
2. Schummers, J., Yu, H. & Sur, M. Tuned responses of astrocytes and their influence on hemodynamic signals in the visual cortex. *Science* **320**, 1638–1643 (2008).
3. Slezak, M. et al. Distinct mechanisms for visual and motor-related astrocyte responses in mouse visual cortex. *Curr. Biol.* **29**, 3120–3127 (2019).
4. Wang, X. et al. Astrocytic Ca²⁺ signaling evoked by sensory stimulation in vivo. *Nat. Neurosci.* **9**, 816–823 (2006).
5. Stobart, J. L. et al. Cortical circuit activity evokes rapid astrocyte calcium signals on a similar timescale to neurons. *Neuron* **98**, 726–735 (2018).
6. Nagai, J. et al. Behaviorally consequential astrocytic regulation of neural circuits. *Neuron* **109**, 576–596 (2021).
7. Adamsky, A. & Goshen, I. Astrocytes in memory function: pioneering findings and future directions. *Neuroscience* **370**, 14–26 (2018).
8. Yu, X. et al. Reducing astrocyte calcium signaling in vivo alters striatal microcircuits and causes repetitive behavior. *Neuron* **99**, 1170–1187 (2018).
9. Kol, A. et al. Astrocytes contribute to remote memory formation by modulating hippocampal-cortical communication during learning. *Nat. Neurosci.* **23**, 1229–1239 (2020).
10. Wahis, J. et al. Astrocytes mediate the effect of oxytocin in the central amygdala on neuronal activity and affective states in rodents. *Nat. Neurosci.* **24**, 529–541 (2021).
11. Volterra, A., Liaudet, N. & Savtchouk, I. Astrocyte Ca²⁺ signalling: an unexpected complexity. *Nat. Rev. Neurosci.* **15**, 327–335 (2014).
12. Thrane, A. S. et al. General anesthesia selectively disrupts astrocyte calcium signaling in the awake mouse cortex. *Proc. Natl Acad. Sci. USA* **109**, 18974–18979 (2012).
13. Curreli, S., Bonato, J., Romanzi, S., Panzeri, S. & Fellin, T. Complementary encoding of spatial information in hippocampal astrocytes. *PLoS Biol.* **20**, e3001530 (2022).
14. Adamsky, A. et al. Astrocytic activation generates de novo neuronal potentiation and memory enhancement. *Cell* **174**, 59–71 (2018).
15. Srinivasan, R. et al. Ca²⁺ signaling in astrocytes from *Ip3r2⁻/⁻* mice in brain slices and during startle responses in vivo. *Nat. Neurosci.* **18**, 708–717 (2015).
16. Paukert, M. et al. Norepinephrine controls astroglial responsiveness to local circuit activity. *Neuron* **82**, 1263–1270 (2014).
17. Vaidyanathan, T. V., Collard, M., Yokoyama, S., Reitman, M. E. & Poskanzer, K. E. Cortical astrocytes independently regulate sleep depth and duration via separate GPCR pathways. *eLife* **10**, e63329 (2021).
18. Corkrum, M. et al. Dopamine-evoked synaptic regulation in the nucleus accumbens requires astrocyte activity. *Neuron* **105**, 1036–1047 (2020).
19. Navarrete, M. et al. Astrocytes mediate in vivo cholinergic-induced synaptic plasticity. *PLoS Biol.* **10**, e1001259 (2012).
20. O'Keefe, J. & Dostrovsky, J. The hippocampus as a spatial map. Preliminary evidence from unit activity in the freely-moving rat. *Brain Res.* **34**, 171–175 (1971).
21. Sosa, M. & Giocomo, L. M. Navigating for reward. *Nat. Rev. Neurosci.* **22**, 472–487 (2021).
22. Xu, H., Baracskay, P., O'Neill, J. & Csicsvari, J. Assembly responses of hippocampal CA1 place cells predict learned behavior in goal-directed spatial tasks on the radial eight-arm maze. *Neuron* **101**, 119–132 (2019).
23. Hollup, S. A., Molden, S., Donnett, J. G., Moser, M. B. & Moser, E. I. Accumulation of hippocampal place fields at the goal location in an annular watermaze task. *J. Neurosci.* **21**, 1635–1644 (2001).
24. Dupret, D., O'Neill, J., Pleydell-Bouverie, B. & Csicsvari, J. The reorganization and reactivation of hippocampal maps predict spatial memory performance. *Nat. Neurosci.* **13**, 995–1002 (2010).
25. Zaremba, J. D. et al. Impaired hippocampal place cell dynamics in a mouse model of the 22q11.2 deletion. *Nat. Neurosci.* **20**, 1612–1623 (2017).
26. Sato, M. et al. Distinct mechanisms of over-representation of landmarks and rewards in the hippocampus. *Cell Rep.* **32**, 107864 (2020).
27. Danielson, N. B. et al. Sublayer-specific coding dynamics during spatial navigation and learning in hippocampal area CA1. *Neuron* **91**, 652–665 (2016).
28. Gauthier, J. L. & Tank, D. W. A dedicated population for reward coding in the hippocampus. *Neuron* **99**, 179–193 (2018).
29. Rubin, A., Geva, N., Sheintuch, L. & Ziv, Y. Hippocampal ensemble dynamics timestamp events in long-term memory. *eLife* **4**, e12247 (2015).
30. Dong, C., Madar, A. D. & Sheffield, M. E. J. Distinct place cell dynamics in CA1 and CA3 encode experience in new environments. *Nat. Commun.* **12**, 2977 (2021).
31. McNamara, C. G., Tejero-Cantero, A., Trouche, S., Campo-Urriza, N. & Dupret, D. Dopaminergic neurons promote hippocampal reactivation and spatial memory persistence. *Nat. Neurosci.* **17**, 1658–1660 (2014).
32. Hainmueller, T. & Bartos, M. Parallel emergence of stable and dynamic memory engrams in the hippocampus. *Nature* **558**, 292–296 (2018).
33. Allegra, M., Posani, L., Gomez-Ocadiz, R. & Schmidt-Hieber, C. Differential relation between neuronal and behavioral discrimination during hippocampal memory encoding. *Neuron* **108**, 1103–1112 (2020).
34. Turi, G. F. et al. Vasoactive intestinal polypeptide-expressing interneurons in the hippocampus support goal-oriented spatial learning. *Neuron* **101**, 1150–1165 (2019).
35. Mederos, S. et al. Melanopsin for precise optogenetic activation of astrocyte-neuron networks. *Glia* **67**, 915–934 (2019).
36. Wang, Y. et al. Accurate quantification of astrocyte and neurotransmitter fluorescence dynamics for single-cell and population-level physiology. *Nat. Neurosci.* **22**, 1936–1944 (2019).
37. Dombeck, D. A., Khabbaz, A. N., Collman, F., Adelman, T. L. & Tank, D. W. Imaging large-scale neural activity with cellular resolution in awake, mobile mice. *Neuron* **56**, 43–57 (2007).
38. Li, N., Daie, K., Svoboda, K. & Druckmann, S. Robust neuronal dynamics in premotor cortex during motor planning. *Nature* **532**, 459–464 (2016).
39. Bromberg-Martin, E. S., Matsumoto, M. & Hikosaka, O. Distinct tonic and phasic anticipatory activity in lateral habenula and dopamine neurons. *Neuron* **67**, 144–155 (2010).
40. Hanks, T. D. et al. Distinct relationships of parietal and prefrontal cortices to evidence accumulation. *Nature* **520**, 220–223 (2015).
41. Maimon, G. & Assad, J. A. A cognitive signal for the proactive timing of action in macaque LIP. *Nat. Neurosci.* **9**, 948–955 (2006).
42. Murakami, M., Vicente, M. I., Costa, G. M. & Mainen, Z. F. Neural antecedents of self-initiated actions in secondary motor cortex. *Nat. Neurosci.* **17**, 1574–1582 (2014).
43. Kim, H. R. et al. A unified framework for dopamine signals across timescales. *Cell* **183**, 1600–1616 (2020).
44. Howe, M. W., Tierney, P. L., Sandberg, S. G., Phillips, P. E. M. & Graybiel, A. M. Prolonged dopamine signalling in striatum signals proximity and value of distant rewards. *Nature* **500**, 575–579 (2013).
45. Mu, Y. et al. Glia accumulate evidence that actions are futile and suppress unsuccessful behavior. *Cell* **178**, 27–43 (2019).
46. Aronov, D., Nevers, R. & Tank, D. W. Mapping of a non-spatial dimension by the hippocampal-entorhinal circuit. *Nature* **543**, 719–722 (2017).
47. Terada, S., Sakurai, Y., Nakahara, H. & Fujisawa, S. Temporal and rate coding for discrete event sequences in the hippocampus. *Neuron* **94**, 1248–1262 (2017).
48. Radvansky, B. A. & Dombeck, D. A. An olfactory virtual reality system for mice. *Nat. Commun.* **9**, 839 (2018).
49. Bittner, K. C., Milstein, A. D., Grienberger, C., Romani, S. & Magee, J. C. Behavioral time scale synaptic plasticity underlies CA1 place fields. *Science* **357**, 1033–1036 (2017).
50. Deemyad, T., Luthi, J. & Spruston, N. Astrocytes integrate and drive action potential firing in inhibitory subnetworks. *Nat. Commun.* **9**, 4336 (2018).

Article

Methods

Animals

Ten PV-tdTomato male mice and one SST-tdTomato male mouse were used for the experiments. The mice were generated by crossing PV-IRES-Cre (B6.129P2-Pvalb[tm1(cre)Arbr]/J, 017320)[51] or SST-IRES-Cre (Sst[tm2.1(cre)Zjh]/J, 013044)[52] mice with Rosa-CAG-LSL-tdT (Ai14; B6.129 S6-Gt(ROSA)26Sor[tm14(CAG-tdTomato)Hze]/J, 007908)[53] mice. Mice (aged 7–8 weeks) were housed under a 12 h–12 h light–dark cycle in cages with running wheels. All of the mice were maintained under pathogen-free conditions in Tecniplast cages, on Teklad sani-chips (ENVIGO) bedding, at 20–24 °C and 40% humidity, and fed Teklad 2918SC (ENVIGO) pellets. The experimental protocols were approved by the Hebrew University Animal Care and Use Committee and met the guidelines of the National Institute of Health guide for the Care and Use of Laboratory Animals.

Surgical procedures

Mice were anaesthetized with isoflurane, and their head was placed in a stereotactic apparatus (Kopf Instruments). The skull was exposed and a small craniotomy was performed. Mice were unilaterally microinjected 400 nl viral vector using the following dorsal CA1 coordinates: anteroposterior, −1.85 mm; mediolateral, +1.4 mm; and dorsoventral, −1.35 mm from bregma. All microinjections were performed using a 10 µl syringe and a 34 gauge metal needle (WPI). The injection volume and flow rate (0.1 µl min⁻¹) were controlled by an injection pump (WPI). After each injection, the needle was left in place for an additional 10 min to allow for diffusion of the viral vector away from the needle track, and was then slowly withdrawn. The craniotomy was sealed with bone wax (Surgical Specialties), and the exposed skull was covered with transparent super-bond (Sun Medical) for cementing an omega-shaped head bar (custom design, 3D printed) anteriorly to the craniotomy site. For postoperative care, the mice were subcutaneously injected with tramadex (5 mg kg⁻¹).

After at least one week of rest, mice were re-anaesthetized with isoflurane in the stereotactic apparatus, and a biopsy punch (Kai Medical) was used to cut a ~2.5 mm diameter craniotomy over the injection site. Aspiration was used to remove the cortical tissue and top most fibres above the right dorsal CA1, and a glass cannula (2.4 mm diameter, 2.5 mm length, no. 0 cover slip bottom; self-fabricated) was inserted into the craniotomy. The skull was covered with opaque super-bond (Sun Medical) for cementing the cannula. An additional layer of dental acrylic was placed to minimize potential physical damage.

Viral vectors

The following viral vector was used: pZac2.1gfaABC1D-cyto-GCaMP6f (Addgene viral prep, 52925-AAV5).

Immunohistochemistry analysis

Mice were transcardially perfused with cold PBS followed by 4% paraformaldehyde in PBS. The brains were extracted, post-fixed overnight in 4% paraformaldehyde at 4 °C and cryoprotected in 30% sucrose in PBS. The brains were sectioned into 40-µm-thick slices using a sliding freezing microtome (Leica SM 2010R) and preserved in a cryoprotectant solution (25% glycerol and 30% ethylene glycol in PBS). Free-floating slices were washed in PBS, incubated for 1 h in blocking solution (1% BSA and 0.3% Triton X-100 in PBS) and incubated overnight at 4 °C with primary antibodies (a full list of the antibodies is provided below) in blocking solution. Slices were then washed with PBS and incubated for 2 h at room temperature with secondary antibodies (a full list of the antibodies is provided below) in 1% BSA in PBS. Finally, the sections were washed in PBS, incubated with 4,6-diamidino-2-phenylindole (1 µg ml⁻¹) and mounted onto slides with mounting medium (Fluoromount-G, eBioscience).

Antibodies. The following primary antibodies were used: chicken anti-GFP (Aveslabs, GFP-1020; 1:200); rabbit anti-NeuN (Cell Signaling Technology, 12943; 1:1,000); guinea pig anti-GFAP (Alomone Labs, AGP-307; 1:200). The following secondary antibodies were used: donkey anti-chicken conjugated to Alexa Fluor 488 (Jackson Laboratories, 703-545-155; 1:500); donkey anti-rabbit conjugated to Alexa Fluor 594 (Jackson Laboratories, 711-585-152; 1:500); donkey anti-guinea pig conjugated to Cy5 (Jackson Laboratories, 706-175-148; 1:500).

Confocal microscopy

Confocal fluorescence images were acquired on the Olympus scanning laser microscope (Fluoview FV1000) using a ×10 air objective. Image analysis was performed using ImageJ (NIH).

Linear treadmill and virtual reality apparatus

Fully awake mice were mounted on top of a linear treadmill with their head bar secured to a custom-made holder under the microscope objective. The treadmill consisted of a 170 cm belt with varying textures, circling two plastic wheels (custom design, 3D printed). To track mouse locomotion, rotations of a rotary encoder (S5-360-236-IE-S-B, US digital) placed in the frontal wheel were measured by Arduino boards. The locomotion data were synchronized with the microscope imaging frames, and translated into movement in the virtual environment. To compensate for sampling errors and belt stretches, an infrared sensor connected to an Arduino board detected a white band on the inner side of the belt and auto-calibrated the virtual reality accordingly on each lap.

A water solenoid valve connected to silicone tubes and a blunt 10 cm needle delivered water rewards in response to TTL commands given by the virtual reality computer through an Arduino board. Licking behaviour was continuously monitored by a capacitance sensor (Atmel Microchip). To synchronize and digitize the valve, infrared and lick signals with the imaging frames, we used a USB-6001 NIDAQ board (National Instruments) and acquired data at 500 Hz using MATLAB. The board recorded TTL signals from the microscope given at the beginning of each frame, as well as TTL commands sent to the valve and TTL inputs originating from the infrared Arduino or lick detector on different analogue channels.

The virtual environments, designed using the Blender game engine, were projected onto a custom-made curved screen. Using a Java graphical user interface, the specific environment of choice and reward locations were determined. The environments consisted of various visual patterns to dissociate different locations in the virtual world. An Arduino board was used to trigger the initiation of the trial.

Behavioural paradigms

Mice were water-restricted and handled for 2–3 days, and we then began training them to run on the linear treadmill to obtain water rewards. Initially, multiple water rewards were spread along the track, and as the mice improved on the course of 7–10 days, we gradually decreased the number of rewards until only one reward was present on each lap. We used two sets of environments, consisting of a treadmill belt with tactile cues and a virtual reality display with visual cues. In the familiar condition, mice were extensively trained in a specific environment, whereas in the new condition we used the other environment, to which the mouse was not previously exposed. We counterbalanced the environments across mice, such that each environment was used both as a familiar and a new one for different mice.

Familiar–new paradigms. Mice were trained extensively in a specific environment (familiar), and then imaged as they were performing the task. After 1–3 days, they were imaged in the new environment. Next, some of them were either trained in the new environment for an additional day and then imaged in the new environment, or re-exposed to the familiar environment and imaged without additional training.

Reward shift paradigm. In the first ten laps, the reward was given at the same location that was used during training (Fa). During the rest of the session, which consisted of 11 more laps, the reward was given at a new location in the same environment (Fb). We omitted the first lap in which the reward was shifted from the analysis. The mice were then trained for an additional session with Fb, and then imaged again in Fb during the task.

Random reward paradigm. Mice were trained in a familiar environment, in which the reward was given at a constant location. During the imaging session, a single water reward was randomly given in one of ten possible locations along the track.

Virtual reality display off paradigm. Mice were trained in a familiar environment. During the imaging session, the virtual reality display was turned off, and the reward was given in the same location as in the training sessions.

Behavioural analysis

We analysed the behaviour of the mouse using custom code run in MATLAB (MathWorks). A lap was defined between each pair of rewards, and the relative location within it was calculated according to the rotary encoder tick count difference between the beginning and end of the lap. For the random reward paradigm, we defined a lap between two infrared signals, that is, a specific location on the belt, and aligned the location according to the previously learnt reward location. We smoothed the raw rotary encoder tick count using a moving average filter (~0.3 s window) and defined movement epochs when the smoothed time series value was >1. Velocity was defined as the derivative of the smoothed time series. We calculated the recent distance run by the mouse by integrating the velocity in a 2 s sliding time-window. When comparing the familiar and new environments, we analysed the first 20 laps in each environment to reduce potential learning effects in the new environment.

Two-photon microscope

Two-photon imaging was performed using the Neurolabware two-photon laser-scanning microscope. Excitation light from a Ti:sapphire laser (Chameleon Vision II, Coherent, and then Chameleon Discovery TPC, Coherent) operated at 920 nm scanned the sample using a 6215 galvometer and a CRS8 resonant mirror (Cambridge Technology). Emitted fluorescence light was detected by GaAsP photo-multiplier tubes (Hamamatsu, H10770-40) after band-pass filtering (Semrock). *xyz* motion control was obtained using motorized linear stages, enabled through an electronic rotary encoder (KnobbyII). We alternately scanned two imaging-planes with an electrically tuneable lens for fast *z*-focusing (Optotune EL-10-30 NIR ETL; f = 100 mm offset lens) to increase the number of astrocytic ROIs per session. A moulding clay ring was mounted between the cannula and the objective to maintain the water reservoir and block external light. The Scanbox software, run on MATLAB, was used for microscope control and image acquisition. All images were acquired using a water-immersion ×16 objective (Nikon, 0.8 NA) with a magnification of 2.8 or 3.4 to obtain 601 μm × 418 μm or 516 μm × 366 μm FOVs. The sampling rate was 15.49 frames per second, that is, 7.745 frames per second for each imaged plane.

Processing calcium imaging data

Motion correction. Calcium imaging movies were corrected for movement in each plane separately using either rigid motion-correction with the sbxaligntool algorithm (Scanbox) or non-rigid motion correction with the NoRMCorre algorithm[54] in MATLAB (MathWorks). When movements were still visible in specific frames, we removed them using the red channel. Specifically, we extracted the mean intensity time series of neuronal ROIs apparent in the red channel and linearly interpolated the signal obtained from each plane. Frames in which an ROI signal was >2 locally scaled median absolute deviations from the local median within a sliding ~3.8 s window in at least 2 ROIs on either plane were excluded from the analysis.

ROI detection. We used the sbxsegmenttool graphical user interface (Scanbox) in MATLAB to semi-automatically detect ROIs on the basis of the motion-corrected videos. The algorithm selects pixels based on their correlation in space and time, such that nearby pixels are defined as an ROI. The correlation threshold was manually set, and was based on the morphology of the ROI, such that different ROIs may belong to the same astrocyte. The segmentation was performed separately for each FOV and for each session.

Signal extraction. The mean fluorescence intensity time series were extracted from the segmented ROIs. The first five samples were removed from the analysis, as well as frames at the end of the video if extensive bleaching was apparent. To synchronize the imaging data with the encoder data, we linearly interpolated the signal obtained from each plane. To obtain $\Delta F/F$ time series for each ROI, we adapted previously published methods[55] for the astrocytic signal. Specifically, we defined the baseline F as the eighth percentile fluorescence value within a ~125 s interval around each sample point. We then subtracted the baseline from each sample, and divided the result by the baseline F. Noisy ROIs, in which there were no apparent calcium transients, were removed from the analysis.

Detection of calcium events. Potential events were first detected based on the $\Delta F/F$ traces; For each ROI, we defined the event threshold as the sum of the mode fluorescence value and its distance from the mean minimal fluorescence value (based on the 100 smallest values). We next obtained potential events based on smoothed $\Delta F/F$ traces (moving median, ~3.9 s window), using the same calculation. We defined an event based on the smoothed traces, only if at least one of the samples within it was also detected as an event based on the original traces, and if it was >260 ms long.

Registration of ROIs across sessions. To image the same FOV across sessions, we used the mean-intensity images of each plane based on the motion-corrected videos obtained during the first imaging session. We used the red channel in which inhibitory neurons were apparent to adjust the objective focus and Optotune parameters until reaching the same FOV. The ROI masks obtained from each session were rigidly aligned using the sbxmatchfields function (Scanbox). Only ROIs that had >20% overlap, and were visually confirmed, were considered as repeated ROIs across 2 consecutive days.

Comparison between astrocytic somata and processes

To differentiate between astrocytic somata and processes, we obtained the mean image from the nine mice that completed the familiar environment paradigm, and superimposed the ROI boundaries on it. We classified the cellular compartment according to the morphology of the ROI. One mouse was excluded from the analysis as it had <10 somata ROIs.

Modulation of astrocytic activity by location or velocity analysis

To obtain concurrent events and event-probability maps, we discretized the either the location or the velocity of the mouse. For location analysis, the track was divided into 10 bins, each 17 cm long, and the last bin in which the reward was given and consumed was removed from further analysis unless otherwise stated. For velocity analysis, we normalized the velocity and obtained arbitrary units within the range 0–1. In both cases, we omitted frames in which the mouse velocity did not exceed the movement criteria (see the 'Behavioural analysis' section).

We then calculated the mean number of concurrent events when examining the entire ROI population, or the event probability when examining single ROIs, per bin in each lap. To obtain the shuffled data activity maps,

Article

we permuted the signal using 1,000 random cyclic shifts, and performed the same analysis as for the real data. The normalized number of concurrent events was calculated by dividing the real data mean number of concurrent events by the shuffled data pooled mean number of concurrent events. To define significant modulation of astrocytic activity by location or velocity, we calculated the linear correlation between these variables from the real and shuffled data. Significance was determined when the Pearson's r obtained from the real data was larger than the 95th percentile of the Pearson's r distribution of the shuffled data.

Astrocytic activity after reward-delivery analysis

We calculated the number of concurrent events as a function of time 7 s after reward delivery in each lap. To determine statistical significance, we permuted the signal using 1,000 random cyclic shifts, and performed the same analysis as for the real data. To define significant modulation of astrocytic activity by location, we calculated the Pearson's linear correlation between these variables from the real and shuffled data. Significance was determined when the correlation coefficient obtained from the real data was lower than the fifth percentile of the shuffled data correlation coefficient distribution.

General linear model

We constructed a simple model to link the astrocytic concurrent event number as a linear function of five behavioural variables: normalized location, time since reward, velocity, recent distance run and licking. We omitted frames in which the mouse velocity did not exceed the movement criteria (see the 'Behavioural analysis' section).

To test the significance of the contribution of the location input to the model performance, we used two approaches. First, we compared the performance of the full model with that of a reduced model fitted on the behavioural variables excluding the location (that is, four predictors only) using a likelihood ratio test accounting for the number of degrees of freedom. Second, we compared the full model performance when it was fitted on the real behavioural data, and compared it with the performance of a similar model, when the location input was shuffled. Specifically, we generated 1,000 realizations of random cyclic shifts of the location data, without changing the rest of the inputs or output. We calculated the coefficient of determination (r^2) between the actual number of concurrent astrocytic events and the model prediction for the real and shuffled-location data models. Significance was defined when the r^2 of the model fitted on the real data was greater than the 95th percentile of the shuffled model r^2 distribution.

For cross-validation, we divided the dataset into 2 s chunks, and pseudorandomly assigned them to one out of ten blocks with equal probability. We used a tenfold cross-validation protocol, in which we trained the model on nine out of the ten blocks, and then tested its performance on the residual block. The activity in each data point was predicted only by a model that did not have this data point in its training set, and used for overall performance estimation. We performed the cross-validation process 1,000 times, using different train–test divisions, for both the five- and four-variable models (that is, with and without location data, respectively). We calculated the r^2 of both models on each realization and compared them. Significance was defined when the r^2 of the full model was greater than the r^2 of the reduced model in more than 95% of the simulations.

ROI spatial information analysis

We calculated the spatial information of astrocytic ROIs using the event probability maps of each ROI as previously described[56]:

$$\text{Spatial information} = \sum_i p_i \left(\frac{r_i}{\bar{r}}\right) \log_2 \left(\frac{r_i}{\bar{r}}\right)$$

where r_i is the calcium event probability of the ROI given that the mouse is in the ith bin; p_i is the probability of the mouse being in the ith bin (samples spent in ith bin/total session samples); $\bar{r}$ is the overall mean calcium event probability; and i running over all of the bins. We then performed 1,000 cyclic permutations of the astrocytic signal, while keeping the behaviour constant, and computed the spatial information for each shuffle. This yielded the P value of the measured spatial information relative to the shuffles.

We also calculated the spatial information based on the mean $\Delta F/F$ maps of each ROI[57], using the same formula with the following changes: r_i is the mean $\Delta F/F$ of the ROI given that the mouse is in the ith bin; $\bar{r}$ is the overall mean $\Delta F/F$; and i running over all of the bins.

Mutual information between repeated ROI analysis

We calculated the mutual information between each pair of repeated ROIs in each environment. We included the acquired astrocytic time series during movement epochs of the mice in the first 20 laps. The pairwise mutual information was considered to be significant when it was higher than the 95th percentile value obtained from 1,000 cyclic permutations of the ROI signals.

Decoding mouse location and velocity

To decode the mouse location or velocity on the basis of astrocytic activity, we trained a linear regression decoder for each mouse separately. We excluded sessions in which mice completed <20 laps. The signal was the binary astrocytic activity traces during movement epochs, and the output was the normalized location along the track or the relative velocity (that is, between 0 and 1). We trained the decoder on 80% of the data, and tested its performance on the remainder, such that the train and test data were from the same session (that is, familiar or new condition). We ran 1,000 train–test sets by dividing the data using a random cut-point. When the predicted location or velocity was out of the range 0–1, it was trimmed (that is, min(prediction, 1), max(prediction, 0)). To determine model significance, we created shuffled data by permuting the signal in a cyclic manner, and performed the same train–test procedure as for the real data. We computed the mean error (that is, the mean difference between the real location and the predicted location) for the decoder trained on the real and shuffled data in each simulation. The model was defined as significant when <50 simulated datasets reached better performance than the real dataset (that is, had a smaller mean error). Confusion matrices were calculated after binning the real and predicted values into ten bins.

Statistical analysis

Data are presented as mean ± s.e.m. unless otherwise indicated. The sample number (n) indicates the number of ROIs or mice in each experiment and is specified in the figure legends. We performed permutation tests by conducting random cyclic shifts of the astrocytic data, and comparing the relevant distribution to the real data. We used two-sided Student's t-tests to compare paired or independent samples, as applicable. Data distribution was assumed to be normal, but this was not formally tested. No statistical methods were used to predetermine sample sizes. The experimenters were not blinded to the experimental conditions, and no randomization was performed. All of the statistical details of the experiments are provided in the main text. $P < 0.05$ was considered to be statistically significant. Analyses were performed using the IBM SPSS statistics software (v.24) and MATLAB.

Reporting summary

Further information on research design is available in the Nature Research Reporting Summary linked to this article.

Data availability

All source data are provided with the paper. All datasets are provided at GitHub (https://github.com/GoshenLab/Astro_imaging/). Source data are provided with this paper.

Code availability

The custom code used in this paper is provided at GitHub (https://github.com/GoshenLab/Astro_imaging/).

51. Hippenmeyer, S. et al. A developmental switch in the response of DRG neurons to ETS transcription factor signaling. *PLoS Biol.* **3**, e159 (2005).
52. Taniguchi, H. et al. A resource of Cre driver lines for genetic targeting of GABAergic neurons in cerebral cortex. *Neuron* **71**, 995–1013 (2011).
53. Madisen, L. et al. A robust and high-throughput Cre reporting and characterization system for the whole mouse brain. *Nat. Neurosci.* **13**, 133–140 (2010).
54. Pnevmatikakis, E. A. & Giovannucci, A. NoRMCorre: an online algorithm for piecewise rigid motion correction of calcium imaging data. *J. Neurosci. Methods* **291**, 83–94 (2017).
55. Dombeck, D. A., Harvey, C. D., Tian, L., Looger, L. L. & Tank, D. W. Functional imaging of hippocampal place cells at cellular resolution during virtual navigation. *Nat. Neurosci.* **13**, 1433–1440 (2010).
56. Markus, E. J., Barnes, C. A., McNaughton, B. L., Gladden, V. L. & Skaggs, W. E. Spatial information content and reliability of hippocampal CA1 neurons: effects of visual input. *Hippocampus* **4**, 410–421 (1994).
57. Radvansky, B. A., Oh, J. Y., Climer, J. R. & Dombeck, D. A. Behavior determines the hippocampal spatial mapping of a multisensory environment. *Cell Rep.* **36**, 109444 (2021).

Additional information
Supplementary information The online version contains supplementary material available at https://doi.org/10.1038/s41586-022-05146-6.
Correspondence and requests for materials should be addressed to Inbal Goshen.
Peer review information *Nature* thanks Caswell Barry and the other, anonymous, reviewer(s) for their contribution to the peer review of this work. Peer reviewer reports are available.
Reprints and permissions information is available at http://www.nature.com/reprints.

Article
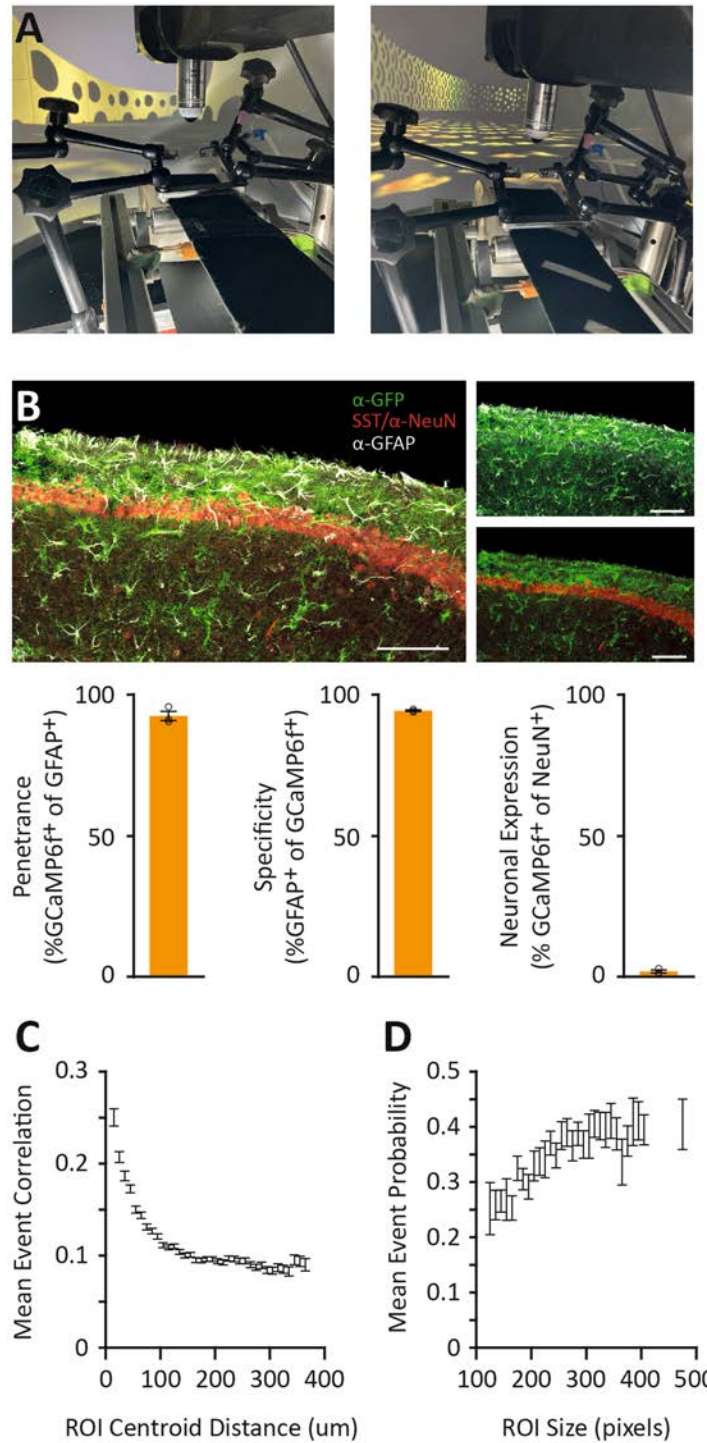
Extended Data Fig. 1 | Apparatus for Imaging Astrocytes in Behaving Mice.
A. Two environments consisting of different belts with tactile cues and virtual reality displays. **B**. Selective expression of GCaMP6f in CA1 astrocytes following injection of AAV-GFAP::cyto-GCaMP6f to an Ai14XSST-Cre mouse. GCaMP6f was expressed in > 92% of CA1 astrocytes (212/230 cells from 3 mice; 92.73% ± 1.65 of GFAP positive cells were also GCaMP6f positive), with > 94% specificity (212/224 cells from 3 mice; 94.58% ± 0.29 of GCaMP6f positive cells were also GFAP positive). Minimal co-localization with SST or PV positive cells or the neuronal marker NeuN was detected (1.65% expression in neurons, 11/668 cells; 1.55% ± 0.54 of GCaMP6f positive cells were also NeuN positive; scale bars: 50 μm). **C**. ROI centroid distance was negatively correlated with the mean pairwise event correlation (pooled data from n = 8 mice). **D**. ROI size was positively correlated with mean event probability (pooled data from n = 8 mice). Data presented as mean±SEM.
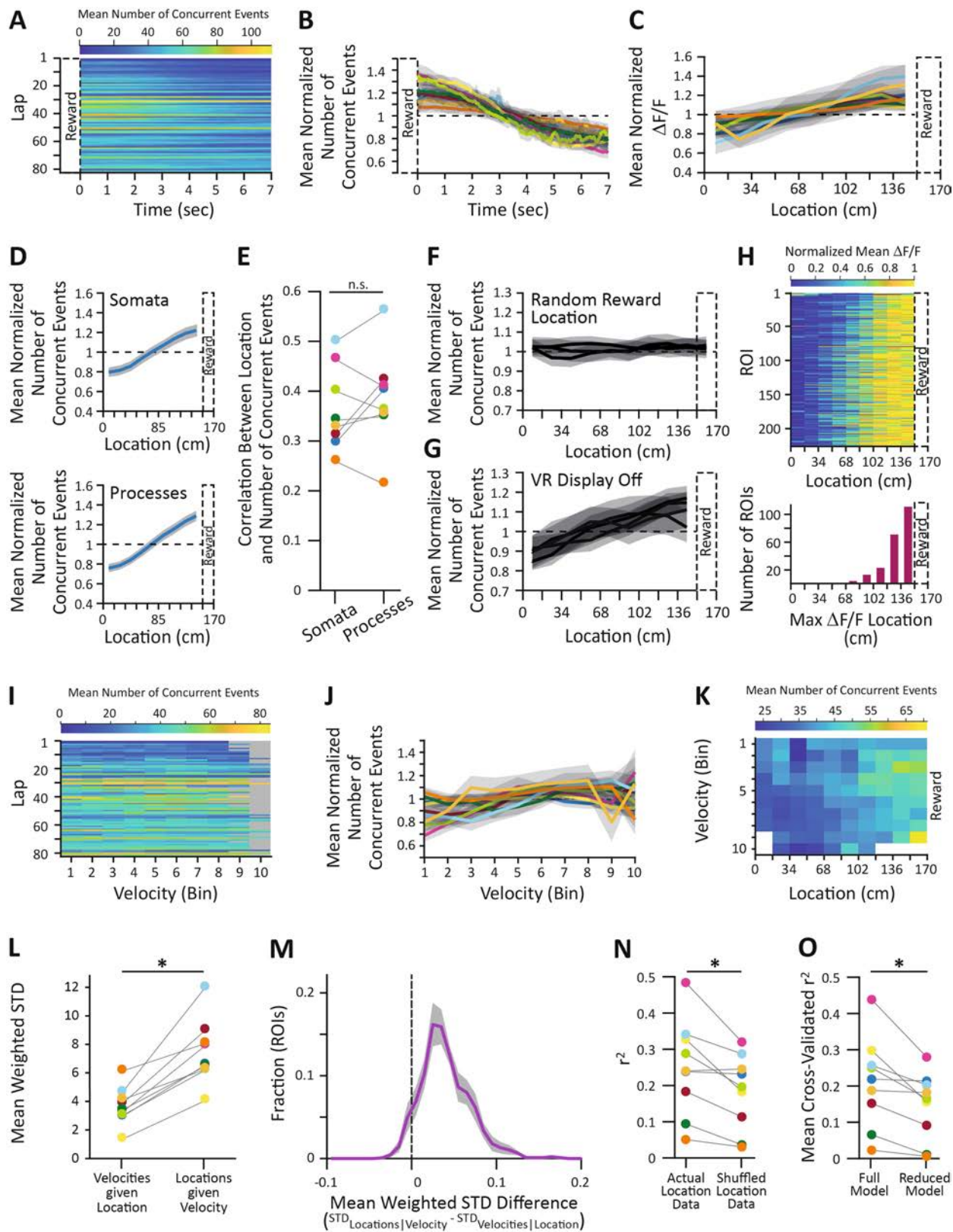
**Extended Data Fig. 2** | See next page for caption.

Article

Extended Data Fig. 3 | See next page for caption.

Extended Data Fig. 3 | Astrocytic Activity Does Not Ramp Towards Rewarding Location in a New Environment. A. The correlation between location and astrocytic activity in repeated active ROIs was significantly higher in the familiar environment compared to the new one (Pearson's r: 0.41 ± 0.03 and 0.2 ± 0.05 in the familiar or new environment, respectively, n = 7 mice, 2-sided paired t-test, $t_{(6)} = 8.04$, $p = 0.0002$). **B**. The repeated active ROI pairs that had significant mutual information (MI) in each environment of the mouse shown in Fig. 3a, b. **C**. The mean proportion of significant MI repeated active ROI pairs in the familiar environment is significantly higher than in the new environment (0.39 ± 0.08 and 0.16 ± 0.04 in the familiar and new environment, respectively, 2-sided paired t-test, n = 7 mice, $t_{(6)} = 2.45$, $p = 0.0495$). **D**. The mean normalized number of concurrent events as a function of location in the familiar environment and (**E**) in the new environment for all active ROIs, not just the repeated ones, in the 7 mice shown in Fig. 3c, d. **F**. The ramping of astrocytic activity is significantly larger in the familiar environment than in the new environment (Pearson's r: 0.44 ± 0.03 and 0.16 ± 0.03 in the familiar or novel environment, respectively, 2-sided independent samples t-test, n = 7 mice, $t_{(12)} = 6.11$, $p = 0.00005$). **G**. Two mice were imaged for the third time in the familiar environment after the exposure to the new environment. The mean normalized number of concurrent events as a function of location shows that ramping is maintained (Pearson's r: 0.31 ± 0.11, 1-sided permutation test, $p < 0.01$). Data presented as mean (bold line) ±SEM (shaded area). Different mice are colour-coded as in Fig. 2d.

A

B

C

D

E

F
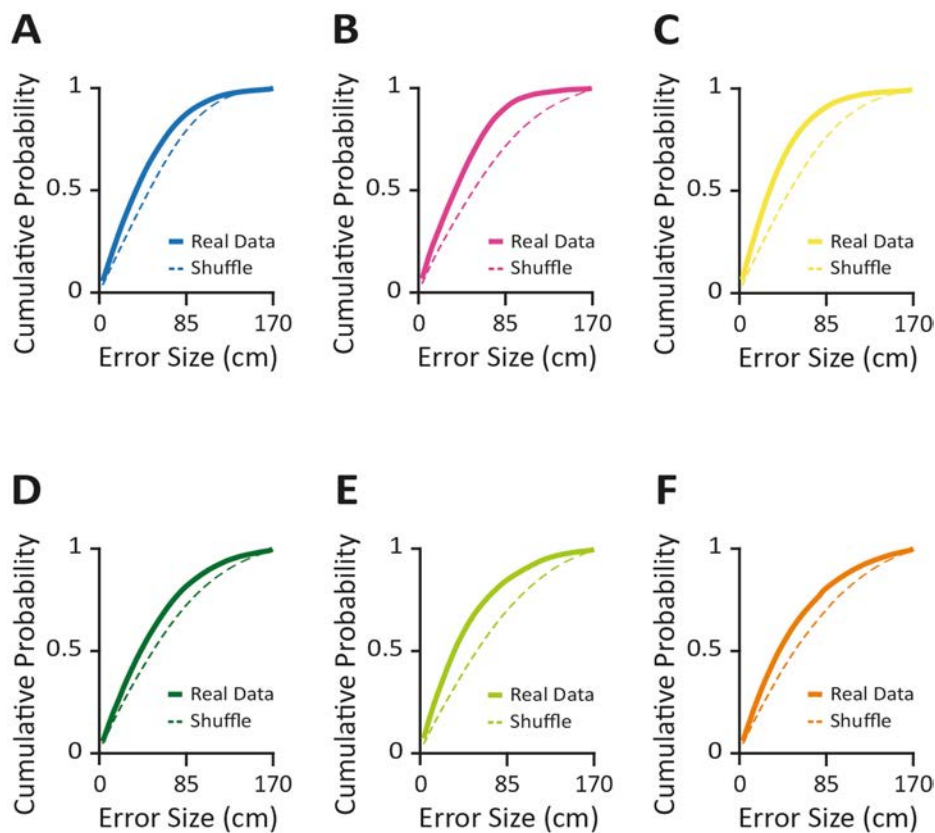
Extended Data Fig. 4 | Performance of Mice Location Decoders in Familiar Environment. A-F. Pooled error cumulative probability plots of the mice that appear in the averaged data in Fig. 4. **A.** Mean error size: 43.7 ± 0.1 and 54.1 ± 0.1, for the decoder trained on the real data and the shuffled data respectively, 1-sided permutation test, p = 0.009). **B.** Mean error size: 41.4 ± 0.2 and 61.1 ± 0.3, for the decoder trained on the real data and the shuffled data respectively, 1-sided permutation test, p = 0.027). **C.** Mean error size: 37.8 ± 0.2 and 56.6 ± 0.2, for the decoder trained on the real data and the shuffled data respectively, 1-sided permutation test, p = 0.009). **D.** Mean error size: 49.6 ± 0.2 and 60.2 ± 0.2, for the decoder trained on the real data and the shuffled data respectively, 1-sided permutation test, p = 0.151). **E.** Mean error size: 43.9 ± 0.3 and 62.6 ± 0.2, for the decoder trained on the real data and the shuffled data respectively, 1-sided permutation test, p = 0.037). **F.** Mean error size: 49.9 ± 0.1 and 62.2 ± 0.2, for the decoder trained on the real data and the shuffled data respectively, 1-sided permutation test, p = 0.061). Data presented as mean (bold line) ±SEM (shaded area). Different mice are colour-coded as in Fig. 2d.